

Hydraulic Fracturing-driven Infrasonic Signals -A New Class of Signal for Subsurface Engineering

Chakravarty Aditya¹, Stenftenagel Jordan¹, Wu Kan¹, Duan Benchun¹, and Misra Siddharth¹

¹Texas A&M University

November 16, 2022

Abstract

Fluid injection into subsurface causes rock deformations, which give rise to mechanical waves in the surrounding rock. This article focuses on the infrasonic signals (2-80 Hz) recorded by hydrophones during a meso-scale (~10 meter) hydraulic fracturing experiment at depth of 1.5 kilometer. We present a full-waveform-based data-driven workflow to map the spatiotemporal evolution of the infrasonic sources produced during hydraulic fracturing. The infrasonic source locations are compared against the simultaneously created microseismic source locations. Orientation of the infrasonic source point cloud strongly agrees with natural fracture orientation, as inferred from the discrete fracture-network modelling. Finally, we arrive at a conceptual model of fluid-injection driven infrasonic generation in subsurface and posit that the reopening of natural fractures is the main mechanism of the infrasonic generation. A joint analysis of signals from microseismicity and infrasonic sources can improve subsurface fracture imaging.

1 Hydraulic Fracturing-driven Infrasound Signals – A New Class of Signal for 2 Subsurface Engineering

3 Aditya Chakravarty¹, Jordan Stenftenagel¹, Kan Wu¹, Benchun Duan², Siddharth Misra^{1,2}

4 ¹ Dept of Petroleum Engineering, Texas A&M University

5 ² Dept of Geology and Geophysics, Texas A&M University

6 Corresponding author: Aditya Chakravarty (aditya.chakravarty@tamu.edu)

7 Key Points:

- 8 • Located the infrasound sources generated during hydraulic fracturing through cross
9 correlation-based grid search.
- 10 • Analyzed the spatiotemporal evolution of the infrasound sources during the hydraulic
11 stimulations and examined their relationship with concurrent microseismicity.
- 12 • Developed a conceptual model for infrasound generation that asserts the reopening of
13 natural fractures as the key mechanism.

14 Abstract

15 Fluid injection into subsurface causes rock deformations, which give rise to mechanical waves in
16 the surrounding rock. This article focuses on the infrasound signals (2-80 Hz) recorded by
17 hydrophones during a meso-scale (~10 meter) hydraulic fracturing experiment at depth of 1.5
18 kilometer. We present a full-waveform-based data-driven workflow to map the spatiotemporal
19 evolution of the infrasound sources produced during hydraulic fracturing. The infrasound source
20 locations are compared against the simultaneously created microseismic source locations.
21 Orientation of the infrasound source point cloud strongly agrees with natural fracture orientation,
22 as inferred from the discrete fracture-network modelling. Finally, we arrive at a conceptual
23 model of fluid-injection driven infrasound generation in subsurface and posit that the reopening
24 of natural fractures is the main mechanism of the infrasound generation. A joint analysis of
25 signals from microseismicity and infrasound sources can improve subsurface fracture imaging.
26

27 Plain Language Summary

28 Underground rocks break and vibrate like a giant subwoofer when fluids are pumped into the
29 earth at sufficiently high injection rates. We analyzed the low-frequency component of recorded
30 hydrophone signals to locate the infrasound energy sources and track their spatiotemporal
31 evolution in the subsurface. These source locations highlight the sections of rock deformation not
32 seen through traditional methods, like microseismic imaging. For imaging underground fracture
33 networks, this new class of infrasound signals is complementary to using signals produced due to
34 microseismicity. A new conceptual model of the fluid-injection driven infrasound generation is
35 presented. The newly developed workflow can aid in imaging subsurface fluid pathways for
36 geothermal and hydrocarbon resource development.

37 **1 Introduction**

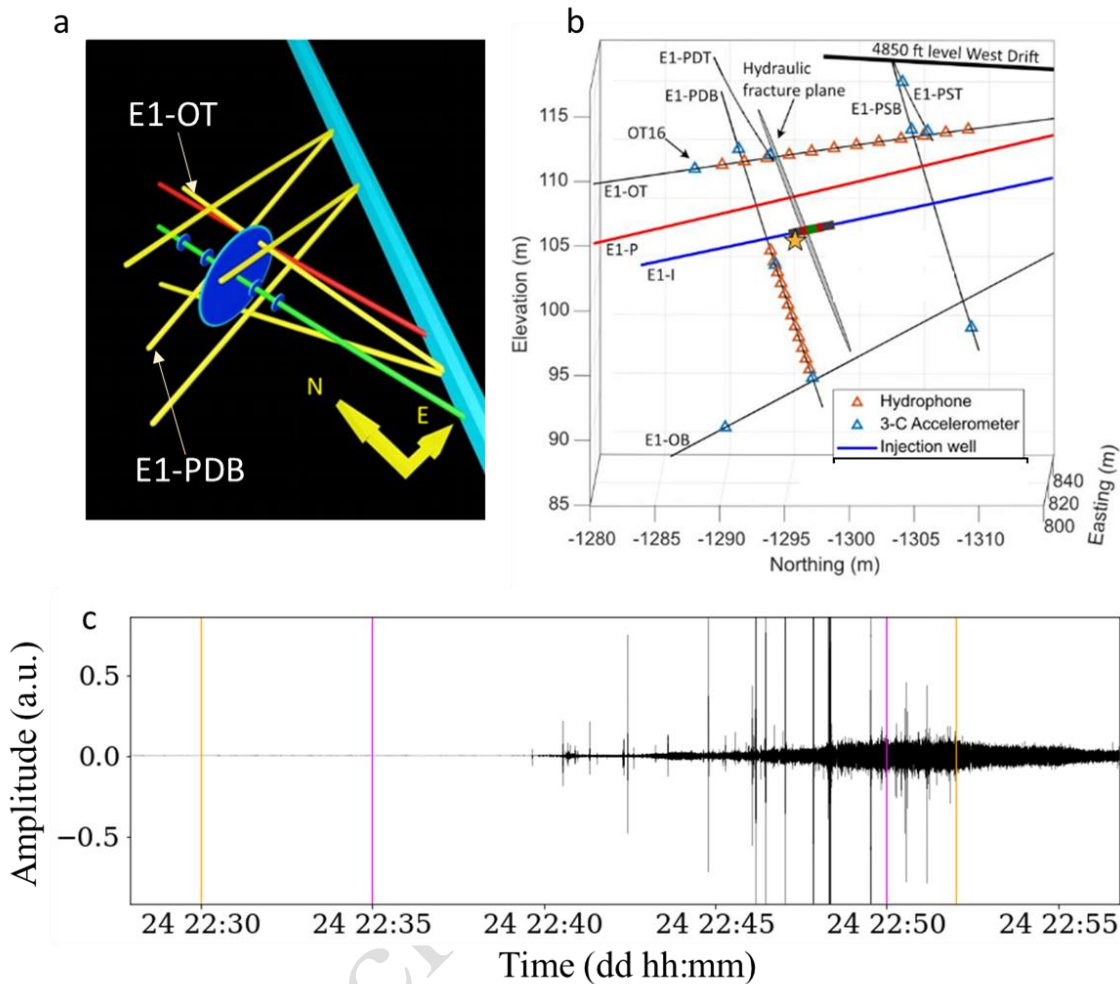
38 **A) Testbed and Experiment Description**

39 The EGS Collab Experiment 1 is a meso-scale (~10 m) hydraulic fracturing testbed situated at
40 the Homestake Gold Mine in Leads, South Dakota at a depth of 1.5 km. The aim of the
41 experiment 1 is detailed characterization of hydraulic fracturing through dense geophysical
42 instrumentation of the stimulated rock volume (Kneafsey et al., 2020 and Chakravarty and Misra,
43 2022). The passive microseismicity during hydraulic stimulation is recorded through array of
44 accelerometers and hydrophones (Figure 1a). The located events determined through manual
45 picking were refined by applying the PhaseNet picker (Zhu and Beroza, 2018) followed with the
46 application of double difference relocation to obtain the final microseismic catalog (Schoenball
47 et al., 2019 and Chai et al., 2020). This catalog, along with distributed fiber optic data and core
48 measurements, which was used to further interpret the fracture network (Fu et al., 2021),
49 constitutes the microseismic point cloud (Figure S7). In this work, we focus on the hydrophone
50 measurements in the low frequency range (2-80 Hz); hereafter, refer as infrasound. Five injection
51 experiments were conducted between 22 and 25 May 2018. The injection rate varied between
52 200 mL/min to 4.5 L/min. The injection and production wells were drilled in the direction of
53 minimum horizontal stress. Table T1 (supplementary text) describes the experiments analyzed
54 here. The hydrophones, spaced 120 centimeters apart, are grouted in place with cement on the
55 monitoring wells. The hydrophones recorded emergent signals in the infrasound frequency
56 (Figure 1c).

57 **B) Monitoring the Fluid-Driven Low-Frequency Subsurface Deformations**

58 Subsurface infrasound can be generated in a wide variety of geological settings where a fluid-
59 driven volumetric process is involved, for example hydrothermal fluid circulation in volcanos,
60 (e.g., Lehr et al., 2019), geysers (e.g., Nayak et al., 2020) and oceanic magmatism (e.g., Sgroi et
61 al., 2009). Neimz et al., 2021 reported borehole tilt signals recorded by broadband seismometers
62 during hydraulic fracturing at the Aspo Hard Rock Laboratory. The tilt magnitude was shown to
63 be directly correlated with injected fluid volume. They concluded that joint analysis of tilt and
64 microseismicity aided fracture growth monitoring. Low-frequency signals from rock
65 deformations have been observed in similar meso-scale rock fracturing experiments like the
66 Aspo Hard Rock Laboratory in Sweden (Zang et al., 2017) and the Grose-Schoen beck in
67 Germany (Boese et al., 2022), and in field-scale hydraulic stimulations in tight sands (Das and
68 Zoback, 2012). However, no further quantitative treatment has been extended for this class of
69 signals so far. Our work focuses on the hydraulic stimulation experiments conducted on a notch
70 located at depth of 50 m on the injection well (Figure 1b) in May 2018. The concurrent
71 geophysical and geomechanical changes in the stimulated volume are captured through densely
72 instruments monitoring boreholes equipped with distributed strain and temperature sensing,

73 electric resistivity, and borehole displacement sensors, apart from the hydrophone and
 74 accelerometer arrays.



75
 76 **Figure 1** – a) Testbed layout of EGS Collab Experiment 1 in Homestake Mine in Leads, South
 77 Dakota. Inset shows the schematic of the well layout, situated at depth of 1500 meters. Red and
 78 green lines represent injection and production wells, respectively, drilled along the minimum
 79 horizontal stress direction. Thick cyan line represents the mine shaft. b) Hydrophone layout. c)
 80 infrasound (2-80 Hz) signal measured by hydrophone OT02 on the 24 May hydraulic fracture
 81 experiment. Time axis represents day: hour: minute. The emergent nature of individual signal
 82 pulses is visibly evident only at much finer time scales. Yellow and magenta vertical line on left
 83 show the start of injection and appearance of first microseismicity, and the other set of lines
 84 mark the last microseismic event and the end of fluid injection. The visible, larger-scale tremor
 85 signal monotonically increases till the pumping stops.

86 **2 Methodology**

87 **A) Data Acquisition**

88 The first step of analysis is the preprocessing of the hydrophone records. Two monitoring wells
89 E1-OT and E1-PDB are equipped with High Tech HTI-96-Min hydrophones. Each well has 12
90 hydrophones spaced two feet apart (Figure 1B). This system has demonstrated high sensitivity in
91 the 2-80 Hz range and applied for quantifying seismic wavefields in oceanic environments
92 (Davidsen et al., 2019 and Lillis et al., 2018). The first step is preprocessing of the hydrophone
93 records. Active seismic sources were being fired during fracturing process and have a very high
94 relative amplitude that overwhelms the underlying passive signal if not clipped. Using the
95 precise timings of active seismic firings, the corresponding time windows were zeroed out in the
96 raw data and replaced with gaussian noise with central tendency statistics matching the
97 neighboring data. As the signals of interest are not impulsive, the source locations identified
98 using first arrival picking methods, like ratio of short-term average to long term average (STA-
99 LTA), are rendered inaccurate. Instead, we located the sources of the fluid injection-driven
100 infrasound using cross correlation-based analysis of full waveforms recorded by the hydrophone
101 array. As the method is data-driven, several filters are applied to minimize the uncertainty
102 associated with the sources.

103 **B) Hydrophone Signal Processing**

104 Following the concatenation and removal of active seismic signals, the signal is detrended and
105 band passed to 2-80 Hz. Since the signals are emergent in nature, we used cross correlation-
106 based grid search approach, which has been widely applied for locating tremor sources in
107 regional and local scales (Wech and Creager, 2008). The input for the algorithm is hydrophone
108 signal, a grid, and a velocity. For the grid dimensions, we used the extent of the hydrophone
109 network with an extension of 30% length in both directions and used an isotropic velocity of 5.5
110 km/second for the compressional wave. A brief description of the rolling window location
111 algorithm is as follows. At every given window, pairwise signals from every station are cross
112 correlated i.e., their similarity is measured as function of displacement of one signal with respect
113 to another. The observed travel time lag as calculated from the correlogram is compared against
114 the calculated theoretical time lag between the station pair using an input velocity model. Within
115 the grid search, the grid node yielding the minimum misfit between modelled and observed
116 difference between objective functions is determined as the source location for the windowed
117 signal. Given a suitable isotropic velocity model, the key parameters determining the source
118 locations of the algorithm are the window length and window overlap. Determining the signal
119 duration of emergent signals is nontrivial due to uncertainty in detecting first arrivals.
120 Application of STA-LTA methods usually lead to overestimating the pulse duration. To get an
121 estimate of the pulse duration, we applied the STA-LTA filter to a sample of hydrophone data
122 from well E1-OT, and then corrected for the overestimation. An average value of one second
123 was obtained as the average pulse duration of the infrasound signals (Figure S1). With this

124 information, a window length is 1 second and window overlap is 0.5 second is chosen for
125 subsequent analysis.

126 **C) Postprocessing Methods on the Grid Search Output**

127 As the location technique is data driven, filters are needed to remove the false positives from
128 results. The filtering steps are described as follows:

129 1.) Correlated noise signals can be highly correlated, which manifests as extremely high
130 normalized cross correlation (CC) coefficients; therefore, the first filter is in form of upper bound
131 of 0.95 on the cross-correlation value. Very loosely correlated signals, have low normalized
132 cross correlation; hence, a lower bound of 0.6 is set. Both the correlated noise and uncorrelated
133 signal windows will yield false positives in the cross-correlation based location. In summary, the
134 windows having normalized cross-correlation coefficients outside the defined bounds (0.6-0.95)
135 are discarded.

136 2.) The second filter is based on the array beam power (Kvaerna and Doornbos, 1985). Using the
137 window lengths and window overlap as used in the location algorithm, the relative power of the
138 hydrophone array was computed throughout the experiments. As a result, both the grid search-
139 based location and beamforming outputs have identical timestamps. The located timestamps
140 (through the grid search) that have normalized beam power lower than the noise floor of the
141 beamforming output is discarded. A threshold value of relative power (0.3) effectively
142 differentiated located and non-located timestamps. In other words, the locations which have a
143 relative power lower the noise floor were removed. The differences between the beam power of
144 the retained and discarded timestamps are shown in Figure S2.

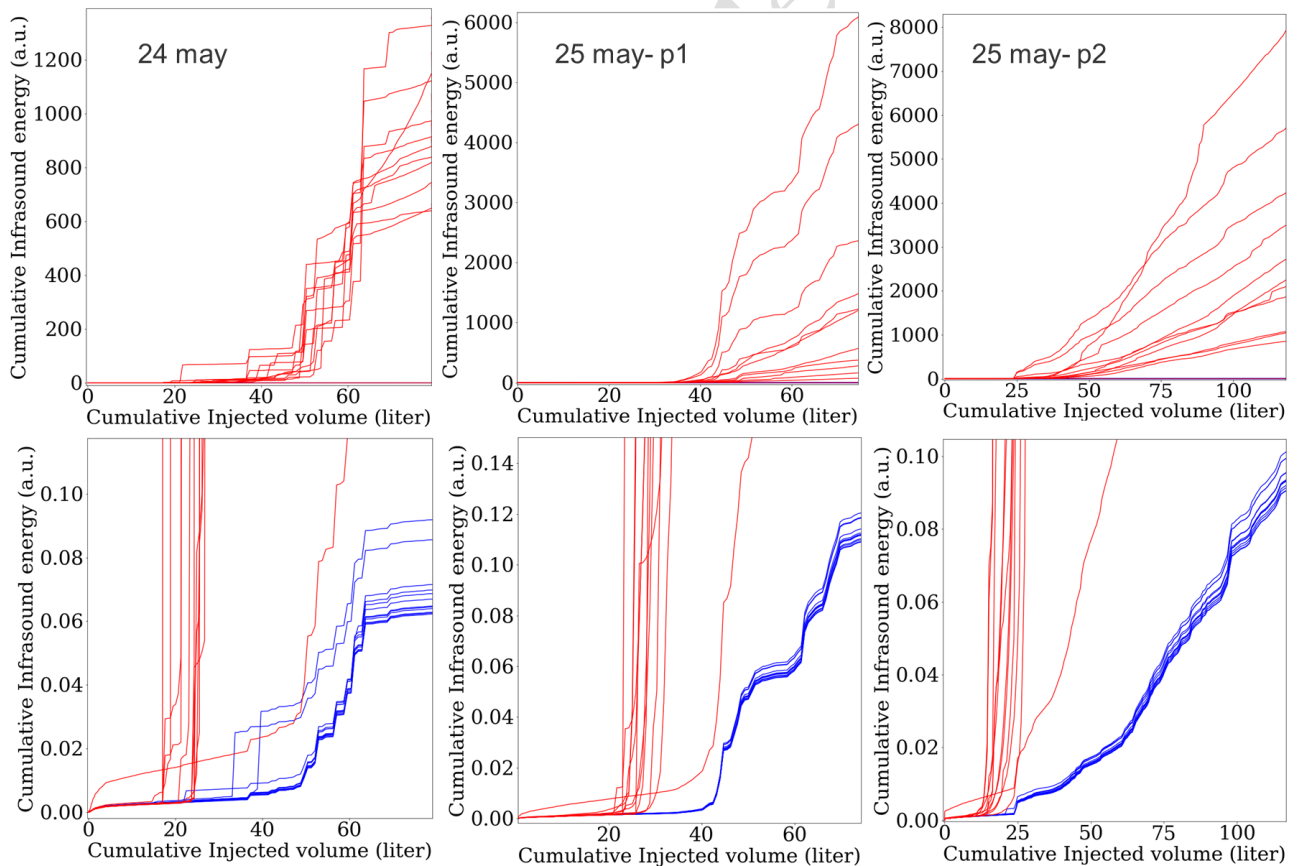
145 3.) The third filter is based on bootstrapping. For every timestep, twenty iterations are performed
146 for the cross-correlation-based locations and in every iteration 5 % of the cross correlograms are
147 randomly removed, and the resulting scatter is considered a measure of location uncertainty. The
148 data points with the highest 10 percent of the scatter values are discarded (for example, in Figure
149 S3). The discarded points represent locations showing maximum scatter in determined locations.

150 4.) The last filter is based on the misfits obtained in the grid search algorithm. The misfit is
151 defined as the difference between the maximum normalized cross-correlation (CC) function and
152 the cross-correlation function corresponding to the located grid node. A large misfit implies
153 weak support from the modelled time lag (from cross correlation) with the observed time lag.
154 50% of the data showing highest misfit values was discarded (Figure S4). Note that the spatial
155 coverage of the source locations shows little change despite losing half the data, underscoring the
156 effectiveness of the misfit filter (Figure S5).

157 **3 Results and Discussion**

158 Two orthogonal hydrophone strings, each consisting of 12 hydrophones recorded the infrasound
159 and infrasound emission during fluid injections. The string E1-OT is perpendicular to the point
160 cloud and intersected by it (Figure S7) whereas the string E1-PDB is sub parallel to the cloud
161 and not intersected by it. As the hydrophones on the well E1-OT are at closer range to the fluid
162 driven deformation, the incident infrasound signal intensity is greater on the E1-OT
163 hydrophones. The signal energy recorded on the string E1-OT is roughly five orders of

164 magnitude greater than string E1-PDB. On 24 May the fluid injection caused hydraulic fracture
 165 propagation until the fracture intersected the production well. The microseismicity subsided as
 166 soon as the intersection with production well caused depressurization. In contrast, the
 167 stimulations of later experiments mostly involved fluid flow through a fractured volume, with a
 168 relatively lower rate of microseismicity. The change from fracture propagation to fluid flow
 169 through fracture is manifest in nature of the cumulative signal energy. Impulsive energy release
 170 indicative of stick slip type of fracture propagation is dominant on 24 May, wherein the energy
 171 release is in discrete bursts, resulting in strong ridges in the cumulative energy curves from all
 172 sensors (Figure 2, left). Fluid flow through fracture conduits generates long-period infrasound
 173 tremors, indicative of long duration energy release that result in progressively smoother
 174 cumulative energy release (Figure 2 C, D). A strong dependence of the cumulative injected
 175 volume with the cumulative signal energy was consistently observed (Supplementary Figure S6)
 176 that implies that the infrasound signals are generated from fluid driven processes. Note that both
 177 hydrophone strings, regardless of their distance from the microseismic cloud (our only proxy for
 178 the fracture location) show this behavior. This implies that although the string closer to the
 179 deformation records a much high energy, the nature of the energy recorded at different locations
 180 is consistent. In other words, both the blue and red curves (corresponding to strings OT and PDB
 181 respectively) have similar morphology while having different scale.



182

183 **Figure 2:** Dependence of fluid injection rate on infrasound energy release. E1-OT is situated
 184 perpendicular to the fractured zone and is intersected by it whereas E1-PDB is lies subparallel to
 185 the fracture and further away than E1-OT. The infrasound energy measured by E1-OT (red)

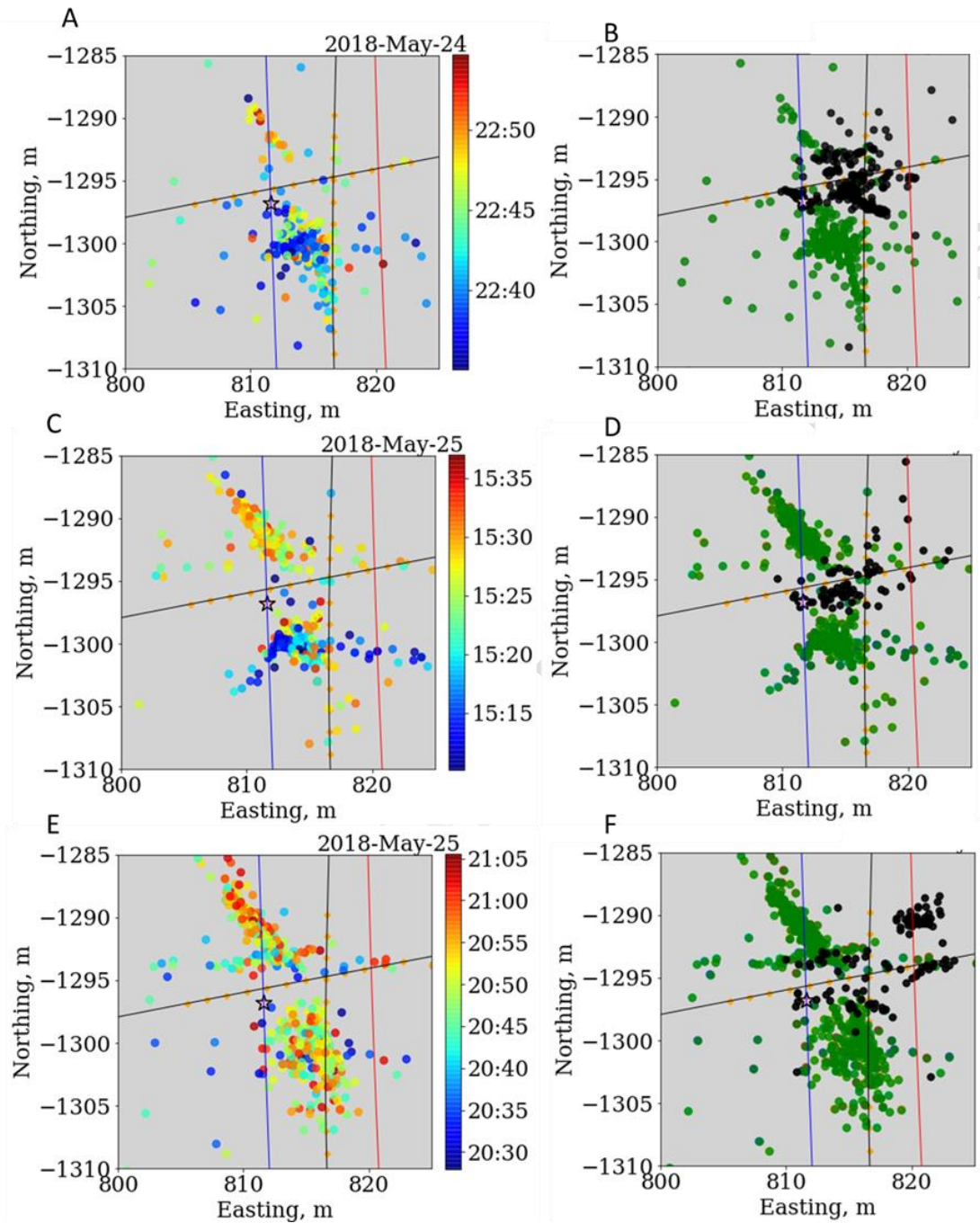
186 hydrophones is five orders of magnitude greater than the distant string E1-PDB (blue). Note that
187 as the experiment proceeds, the gradient of cumulative infrasound energy for the both the
188 hydrophone strings becomes progressively smoother. Impulsive energy release indicative of stick
189 slip type of fracture propagation is dominant on 24 May, wherein the energy release is in discrete
190 bursts, resulting in strong ridges in the cumulative energy curves from all sensors. Fluid flow
191 through fracture conduits generates long-period infrasound tremors, indicative of long duration
192 energy release. This transition suggests a regime change from fluid-driven fracture propagation
193 to fluid flow through fractured conduits.

194 On 22 and 23 May the maximum injection rates were 200 mL/min and 400 mL/min respectively
195 and only very weak infrasound signals were obtained. Signals with sufficiently high signal to
196 noise ratio were obtained for 24 May, and the two parts of 25 May wherein the maximum
197 injection rate was 4.5 L/min, the highest values in current experiment. Figure 3 shows the
198 location of the infrasound sources. After applying the filters to the initial result from cross
199 correlation-based grid search, a total of 322, 818, and 1117 infrasound source locations were
200 obtained for the three stimulations respectively.

201 **A) Spatiotemporal Evolution of Infrasound Sources and Microseismicity**

202 Figure 3 shows the spatiotemporal evolution of the infrasound source locations. On 24th, early
203 time (up to 22:40 UTC) sources spread perpendicular to the injection well (Figure 3a). Around
204 22:45 UTC, the sources are concentrated along a lineament sub parallel to the injection well. The
205 later events are oriented along the same direction but have migrated northward from the injection
206 point. Simultaneous microseismicity is shown in Figure 3b. The microseismic point cloud
207 situated at $x=815$ m overlays and extends the late-time infrasound source point cloud which is
208 situated north of the injection point. The sources on 25th part 1 (Figure 3c) show a less diffuse
209 distribution than previously seen. The early time sources lie along an east-west trend (i.e., sub-
210 perpendicular to injection well) south of injection point. A relatively sparse linear trend is also
211 formed by later events on the north of injection point. Two subparallel lineaments in east-west
212 direction are observed. At the start of injection on 25th part 2 (Figure 3e), infrasound sources fall

213 on the previously described two lineaments on either side of injection point, being sub
 214 perpendicular to the injection well. The latter events are aligned sub parallel to the injection well.



215
 216 **Figure 3:** a,b) May 24; c,d) May 25 part 1; and e,f) May 25 part 2. Colored points show
 217 infrasound while black points show the simultaneously recorded microseismicity. Blue and red
 218 lines indicate injection and production wells respectively. Pink star on the injection well E1-I
 219 marks the injection point. Black line subparallel to injection and monitoring wells is hydrophone
 220 string E1-PDB, and sub horizontal line is string E1-OT. Orange squares overlain on lines mark
 221 the hydrophone sensors emplaced in the monitoring wells.

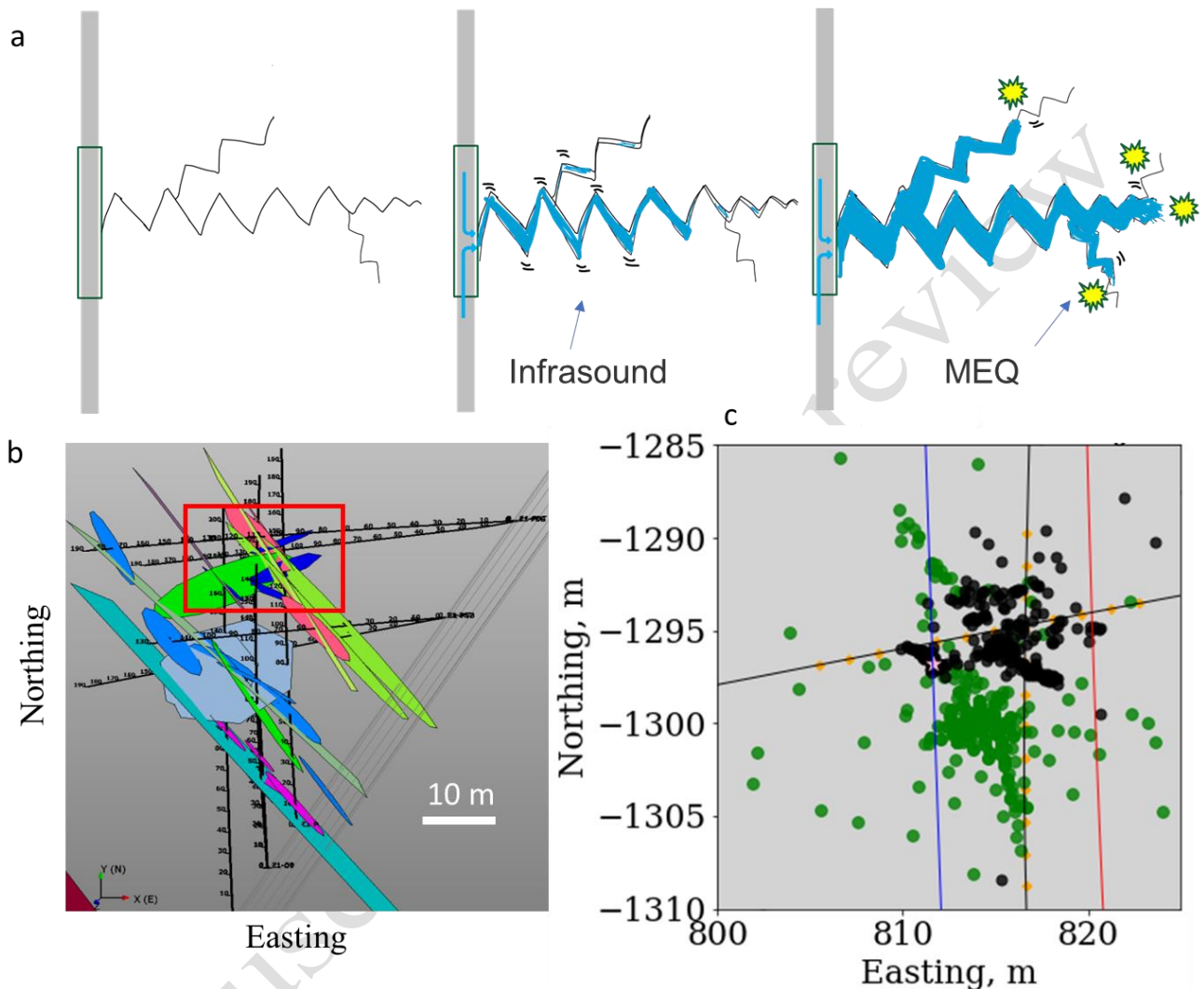
222 **B) Joint analysis of Discrete Fracture Network and Infrasound Source Locations**

223 Fusion of complimentary imaging methods like active and passive seismic can improve fracture
224 imaging (e.g., Chakravarty and Misra, 2021). Similarly, the joint analysis of high and low
225 frequency components of deformation captures information about fracture phenomena that is
226 absent in those from standalone methods, such as microseismic analysis. The high frequency
227 microseismicity usually corresponds to the shear slippage along the fractures leading to fracture
228 propagation. In case of fluid injection-induced seismicity there is also a significant volumetric
229 component in the seismic moment at much higher, microseismic frequency range, that is
230 reflected by a significant percentage of the isotropic component in the microearthquake moment
231 tensors (Martinez-Garzon et al., 2017). The lithology of the EGS Collab experiment 1 testbed is
232 naturally fractured, highly metamorphosed phyllite. Whether intact or fractured, as fluid is
233 pumped in a fractured rock, the injection causes crack opening. This pressurized fluid ‘inflates’
234 (or deflates, in case of drainage) the crack volume, the volume behaves like a diaphragm
235 generating mechanical waves. Whereas in microseismicity, S-wave energy is predominantly
236 generated, it is assumed that crack opening is dominantly tensile and generates P-wave energy.
237 These low frequency P-waves are then recorded by the surrounding the array of pressure
238 transducers. Using the example of fluid injection in a fractured rock, we present our conceptual
239 model of fluid-driven infrasound generation in Figure 4a. In this model the fluid front is driving
240 the fracture propagation as it shears the rock fabric, creating high-frequency shear motion
241 (microseismicity). In the wake of the fluid front, the pressurized volume emanates low frequency
242 P-waves.

243 The discrete fracture network showing the orientation and extent of the interpreted natural
244 fractures is shown in Figure 4b. Dominant orientation of the fractures is 140° (CCW from east).
245 These natural fractures, oriented subparallel to least horizontal stress direction (and the injection
246 well) are the most favorable candidates for the fluid pressurization as described above (Figure
247 4c). The infrasound source cloud has two principal directions: dominant orientation being 140°
248 (CCW from east) and the minor direction being the east-west trending section. The east west
249 trending fracture network was created due to hydraulic fracturing, as shown in Figure 3b. We
250 also note that a large section of the infrasound activity lies away from the production well. The
251 difference in locations of microseismicity and infrasound underscore the different fluid pathways
252 possible. The section described by microseismicity is where the critically stressed cracks are
253 mobilized by fluid interactions, generating shear motion. On the other hand, sections of
254 infrasound activity represent the pressurized zones, most likely reopened natural fractures, and
255 generate low frequency compressional motion. Such observations also highlight the geometrical
256 complexity of the stimulated rock volume in contrast to the ideal penny-shaped fracture as
257 pictured in Figure 1a. Operationally, this observation corroborates high amounts of fluid leak off

258 into the fractured formation, seen from large differences between the injected and produced
259 water volume.

260



261

262 **Figure 4:** a) Schematic representation of the fluid-injection driven infrasound and microseismic
263 energy release in a naturally fractured rock volume. MEQ's are microseismic events. b)
264 Comparison with microseismic and discrete fracture network (DFN). The DFN figure is adapted
265 from a model generated after the stimulation experiments (Schwering et al., 2019), wherein the
266 authors used data from borehole optical and acoustic cameras to ascertain the dip, strike and
267 aperture of the natural fractures encountered in the monitoring wells. The interpreted network
268 shows the orientation of pre-existing natural fractures in the testbed, with large majority of the
269 features inclined at 140° counterclockwise from east. Red box highlights the area of located
270 infrasound activity. c) Their combined location cloud shows strong agreement with overall
271 orientation inferred from the DFN.

272

273

274

275 4 Conclusions

276 The low-frequency (2-80 Hz) hydrophone signals captured during a 1.5 km deep meso-scale
277 (~10 m) hydraulic fracturing experiment is analyzed to locate previously undetected infrasound
278 sources. The infrasound detected by the hydrophone array is driven by fluid injection. A total of
279 322, 818, and 1117 infrasound source locations were obtained for the three stimulations
280 respectively. Impulsive energy release at earlier stages corresponded to fracture propagation,
281 while a smoother release at later stages of stimulation corresponds to tremor like motions
282 generated from fluid flow in conduits. Infrasound signals of usable signal to noise ratio are
283 produced only at relatively high fluid injection rates. The infrasound is emergent signal so first
284 arrival picking from threshold-based methods is rendered inaccurate. Therefore, a data-driven
285 cross-correlation-based grid search was applied to locate the infrasound source locations. Four
286 filtering steps were designed and applied to improve the source location algorithm. The filters
287 are thresholds based on the array power, thresholds based on the misfit in the cross-correlation
288 based grid searching, scatter in locations obtained from station bootstrapping, and upper and
289 lower bounds on the normalized cross correlation coefficient. Once the final locations of
290 infrasound sources were obtained, the spatiotemporal evolution of the source locations over three
291 episodes of fluid injection was analyzed. It is observed that the infrasound hotspots shifted
292 around the fluid injection point over the course of fracturing operations. Whereas some locations
293 produce exclusively one type of signal. Some locations can produce both infrasound and
294 microseismicity. Those locations have overlap- show both high and low frequency deformation
295 from fluid injection. Based on the spatiotemporal evolution of the infrasound sources in
296 comparison to the microseismic sources and the discrete fracture network model, we conclude
297 that the pressurized fluid inflates or deflates a fractured volume depending on whether there is
298 injection or drainage- and the stimulated volume generates compressional waves.

299
300 Based on the discrete fracture network model of the testbed before fracturing, there exists a
301 strong agreement between the fracture orientations and infrasound source locations. The
302 pressurization of natural fractures appears to be the most likely mechanism for generating
303 infrasound. As infrasound corresponds to fluid flow, our observations show that a large portion
304 of the injected fluid is diverted away from the intended location i.e., the production well. A key
305 caveat associated with our location method is that the output is in two dimensions.
306 It is well understood that microseismicity represents only a minuscule portion of the input
307 hydraulic energy and only partly images the fracture network. The joint analysis of infrasound
308 and microseismic encapsulates frequencies on the observable bounds of acquisition
309 instrumentation (2 Hz to 15000 Hz). As a result, both high and low frequency fracturing
310 phenomena driven by fluid injection are captured. The joint data reflects fluid injection-induced
311 subsurface deformation that lies on a continuum - with one end representing of high frequency,
312 small-scale shear slippage on fractures and the other end representing low frequency, large-scale
313 void volume dilation or contraction. It is hence concluded that microseismicity and infrasound
314 signals contain complementary information about rock deformation due to fluid injection, and
315 their joint analysis renders a more complete picture of the stimulated fractures in subsurface.

316
317
318
319
320

321 **Acknowledgments**

322 This material is based upon work supported by the U.S. Department of Energy, Office of
323 Science, Office of Basic Energy Sciences, Chemical Sciences Geosciences, and Biosciences
324 Division, under Award Number DE-SC0020675 and the Texas A&M TRIAD funding. The
325 authors acknowledge the efforts of the EGS collab team for conceptualizing and executing the
326 experiments and hosting the open-source data. The authors are grateful to Texas A&M High
327 Performance Research Computing staff for their support.

328

329 **Open Research**

330

331 The data used in this study is publicly available and can be accessed from the Geothermal Data
332 Repository GDR (gdr.openei.org). The hydrophone, continuous microseismic data and
333 microearthquake catalog are available at <https://gdr.openei.org/submissions/1166>. Hydraulic
334 fracturing operational data is available at <http://gdr.openei.org/submissions/1229>. Data
335 processing and visualization done in Python.

336

337 **References**

338

339 1. Boese, C. M., Kwiatak, G., Fischer, T., Plenkers, K., Starke, J., Blümle, F., Janssen, C., &
340 Dresen, G. (2022). Seismic monitoring of the STIMTEC hydraulic stimulation experiment
341 in anisotropic metamorphic gneiss. *Solid Earth*, 13(2), 323–346.
342 <https://doi.org/10.5194/SE-13-323-2022>

343

344 2. Chai, C., Maceira, M., Santos-Villalobos, H. J., Venkatakrishnan, S. V., Schoenball, M.,
345 Zhu, W., Beroza, G. C., & Thurber, C. (2020). Using a Deep Neural Network and Transfer
346 Learning to Bridge Scales for Seismic Phase Picking. *Geophysical Research Letters*,
347 47(16). <https://doi.org/10.1029/2020GL088651>

348

349 3. Chakravarty, A., & Misra, S. (2021). Hydraulic fracture mapping using wavelet-based
350 fusion of wave transmission and emission measurements. *Journal of Natural Gas Science
351 and Engineering*, 96, 104274. <https://doi.org/10.1016/J.JNGSE.2021.104274>

352

353 4. Chakravarty, A., & Misra, S. (2022). Unsupervised learning from three-component
354 accelerometer data to monitor the spatiotemporal evolution of meso-scale hydraulic
355 fractures. *International Journal of Rock Mechanics and Mining Sciences*, 151, 105046.
356 <https://doi.org/10.1016/J.IJRMMS.2022.105046>

357

358 5. Das, I., & Zoback, M. D. (2013). Long-period long-duration seismic events during
359 hydraulic stimulation of shale and tight-gas reservoirs - Part 2: Location and
360 mechanisms. *Geophysics*, 78(6).

- 361
362
363
364
365
366
6. Davidsen, J. G., Dong, H., Linné, M., Andersson, M. H., Piper, A., Prystay, T. S., Hvam, E. B., Thorstad, E. B., Whoriskey, F., Cooke, S. J., Sjursen, A. D., Rønning, L., Netland, T. C., & Hawkins, A. D. (2019). Effects of sound exposure from a seismic airgun on heart rate, acceleration and depth use in free-swimming Atlantic cod and saithe. *Conservation Physiology*, 7(1). <https://doi.org/10.1093/CONPHYS/COZ020>
- 367
368
369
370
371
372
373
374
7. Fu, P., Schoenball, M., Ajo-Franklin, J. B., Chai, C., Maceira, M., Morris, J. P., Wu, H., Knox, H., Schwering, P. C., White, M. D., Burghardt, J. A., Strickland, C. E., Johnson, T. C., Vermeul, V. R., Sprinkle, P., Roberts, B., Ulrich, C., Guglielmi, Y., Cook, P. J., ... Kneafsey, T. J. (2021). Close Observation of Hydraulic Fracturing at EGS Collab Experiment 1: Fracture Trajectory, Microseismic Interpretations, and the Role of Natural Fractures. *Journal of Geophysical Research: Solid Earth*, 126(7), e2020JB020840. <https://doi.org/10.1029/2020JB020840>
- 375
376
377
378
379
8. Kneafsey, T. J., Blankenship, D., Dobson, P. F., Morris, J. P., White, M. D., Fu, P., et al. (2020). The EGS Collab Project: Learnings from Experiment 1. In Proceedings 45th 311 Workshop on Geothermal 312 Reservoir Engineering, 15 p., Stanford University, Stanford, California
- 380
381
382
383
9. Kvaerna T, D J Doornbos. An integrated approach to slowness analysis with arrays and three-component array data. Semiannual Technical Summary, 1 October 1985-31 March 1986. Kjeller, Norway: Sci. Rept. No. 2-85/86, NORSAR,1986.
- 384
385
386
387
10. Lehr, J., Eckel, F., Thorwart, M., & Rabbel, W. (2019). Low-Frequency Seismicity at Villarrica Volcano: Source Location and Seismic Velocities. *Journal of Geophysical Research: Solid Earth*, 124(11), 11505–11530. <https://doi.org/10.1029/2018JB017023>
- 388
389
390
391
392
11. Lillis, A., Caruso, F., Mooney, T. A., Llopiz, J., Bohnenstiehl, D., & Eggleston, D. B. (2018). Drifting hydrophones as an ecologically meaningful approach to underwater soundscape measurement in coastal benthic habitats. *JEA*, 2(1), 1–1. <https://doi.org/10.22261/JEA.STBDH1>
- 393
394
395
396
12. Martínez-Garzón, P., Kwiatek, G., Bohnhoff, M., & Dresen, G. (2017). Volumetric components in the earthquake source related to fluid injection and stress state. *Geophysical Research Letters*, 44(2), 800–809. <https://doi.org/10.1002/2016GL071963>
- 397
398
399
13. Nayak, A., Manga, M., Hurwitz, S., Namiki, A., & Dawson, P. B. (2020). Origin and Properties of Hydrothermal Tremor at Lone Star Geyser, Yellowstone National Park,

- 400 USA. *Journal of Geophysical Research: Solid Earth*, 125(12), e2020JB019711.
401 <https://doi.org/10.1029/2020JB019711>
- 402
- 403 14. Niemez, P., Dahm, T., Milkereit, C., Cesca, S., Petersen, G., & Zang, A. (2021). Insights Into
404 Hydraulic Fracture Growth Gained From a Joint Analysis of Seismometer-Derived Tilt
405 Signals and Acoustic Emissions. *Journal of Geophysical Research: Solid Earth*, 126(12),
406 e2021JB023057. <https://doi.org/10.1029/2021JB023057>
- 407
- 408 15. Schoenball, M., Ajo-Franklin, J. B., Blankenship, D., Chai, C., Chakravarty, A., Dobson, P.,
409 Hopp, C., Kneafsey, T., Knox, H. A., Maceira, M., Robertson, M. C., Sprinkle, P.,
410 Strickland, C., Templeton, D., Schwering, P. C., Ulrich, C., & Wood, T. (2020). Creation of
411 a Mixed-Mode Fracture Network at Mesoscale Through Hydraulic Fracturing and Shear
412 Stimulation. *Journal of Geophysical Research: Solid Earth*, 125(12), e2020JB019807.
413 <https://doi.org/10.1029/2020JB019807>
- 414
- 415 16. Schwering, P. C., Doe, T. W., Roggenthen, W. M., Neupane, G. H., Johnston, H., Dobson,
416 P. F., Ulrich, C., Singh, A., Uzunlar, N., and C. Reimers. "Deterministic Discrete Fracture
417 Network (DFN) Model for the EGS Collab Project on the 4850 Level of the Sanford
418 Underground Research Facility (SURF)." Paper presented at the 54th U.S. Rock
419 Mechanics/Geomechanics Symposium, physical event cancelled, June 2020.
- 420 17. SgROI, T., Montuori, C., Favali, P., & Agrusta, R. (2009). Low-frequency seismic signals
421 recorded by OBS at Stromboli volcano (Southern Tyrrhenian Sea). *Geophysical Research
422 Letters*, 36(4). <https://doi.org/10.1029/2008GL036477>
- 423
- 424 18. Wech, A. G., & Creager, K. C. (2008). Automated detection and location of Cascadia
425 tremor. *Geophysical Research Letters*, 35(20), 20302.
426 <https://doi.org/10.1029/2008GL035458>
- 427
- 428 19. Zang, A., Stephansson, O., Stenberg, L., Plenkers, K., Specht, S., Milkereit, C., Schill, E.,
429 Kwiatek, G., Dresen, G., Zimmermann, G., Dahm, T., & Weber, M. (2017). Hydraulic
430 fracture monitoring in hard rock at 410 m depth with an advanced fluid-injection
431 protocol and extensive sensor array. *Geophysical Journal International*, 208(2), 790–813.
432 <https://doi.org/10.1093/GJI/GGW430>
- 433
- 434 20. Zhu W, Beroza GC. PhaseNet: A deep-neural-network-based seismic arrival-time picking
435 method. *Geophys J Int*. 2019;216(1):261-273. doi:10.1093/gji/ggy423

Hydraulic Fracturing-driven Infrasonic Signals – A New Class of Signal for Subsurface Engineering

Aditya Chakravarty¹, Jordan Stenftenagel¹, Kan Wu¹, Benchun Duan², Siddharth Misra^{1,2}

¹ Dept of Petroleum Engineering, Texas A&M University

² Dept of Geology and Geophysics, Texas A&M University

Corresponding author: Aditya Chakravarty (aditya.chakravarty@tamu.edu)

Contents of this file

Text S1 to S7

Tables S1

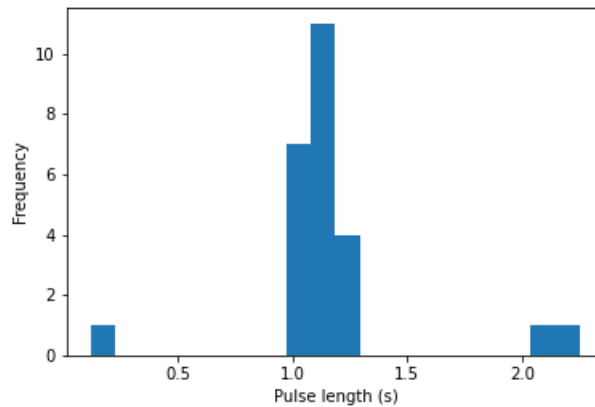


Figure S1: Histogram of infrasound pulse durations for 24 May hydrophone OT-03 (sampling rate = 200 Hz) obtained by applying STA LTA filter (short window = 300 pts, long window = 3000 pts)

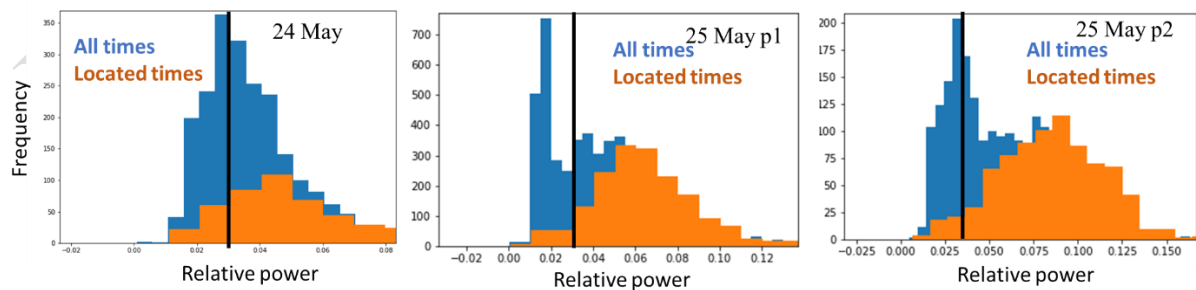


Figure S2: Histogram of beam power values showing variation of power values between located times (orange) and all data (blue). A threshold of 0.3 is determined as the beam power noise floor.

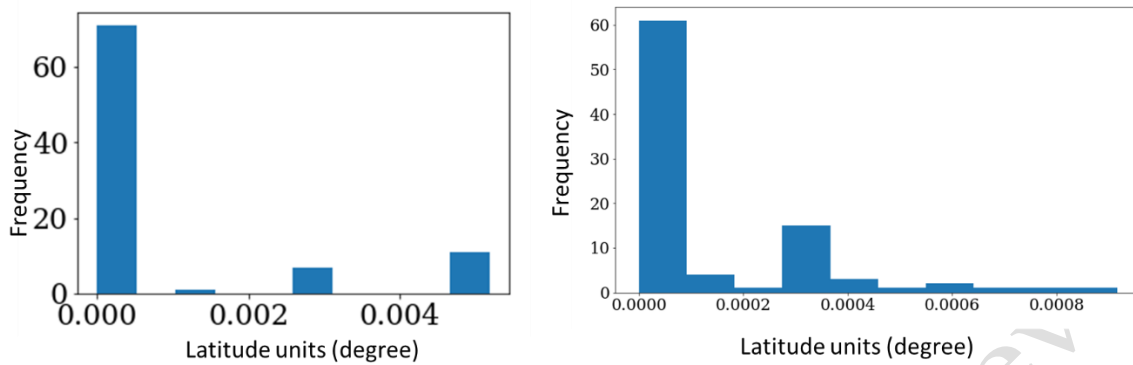


Figure S3: Horizontal scattering obtained from station bootstrapping, shown here for 24 May (left) and 25 May p1 (right). The highest 10% of scattered values are discarded.

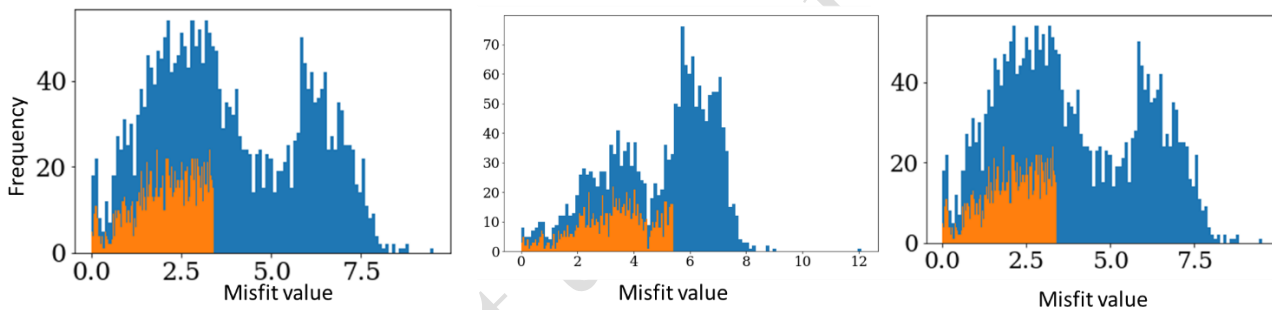


Figure S4: Histograms of misfit values obtained for 24, 25p1 and 25p2 experiments (left, center, and right respectively). Blue bars represent all misfit values and orange bars represent data with 50% of highest misfit values removed).

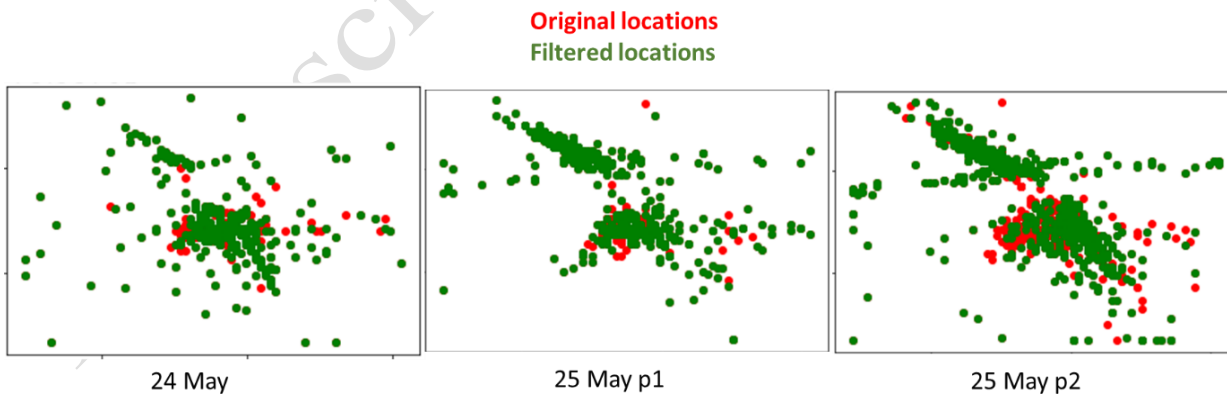


Figure S5: Effect of applying the misfit filter. Pre and post filtered data shown in red and green respectively.

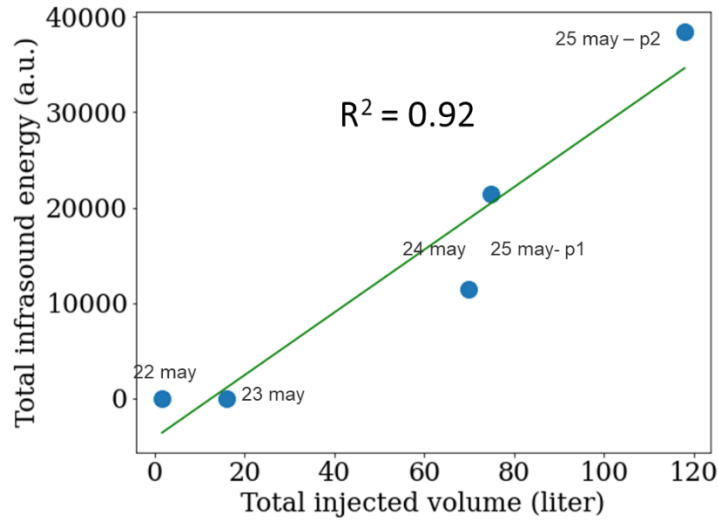


Figure S6: Dependence of cumulative infrasound (2-80 Hz) measured by combined hydrophone arrays (located on the monitoring wells E1-OT and E1-PDB).

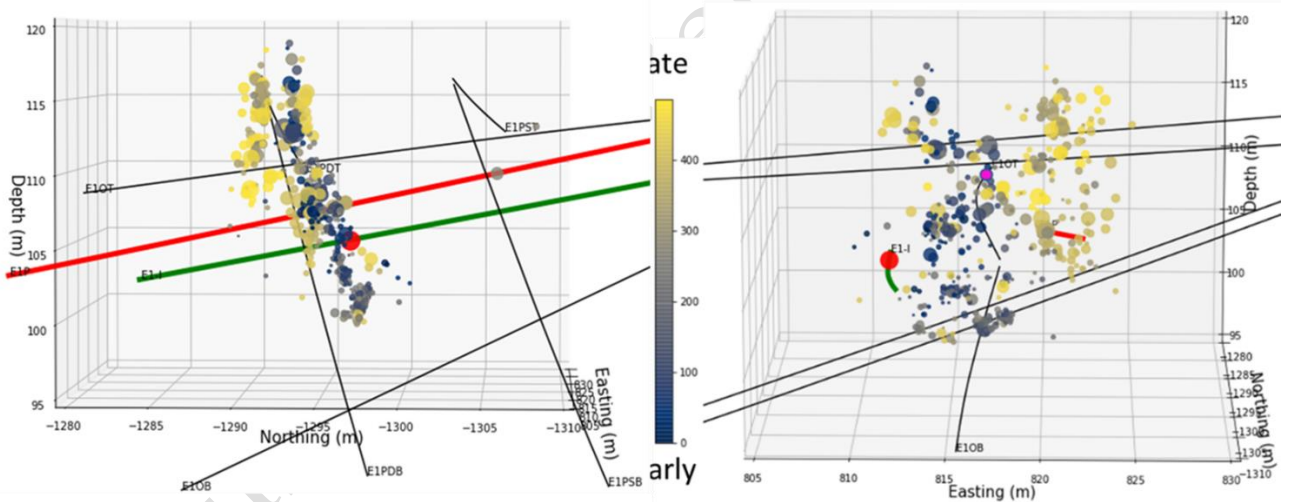


Figure S7: Relative orientation of wells E1-OT and E1-PDB microseismic cloud (combined 24 May and 25 May) with the injection and production wells (green and red, respectively).

Day (2018)	Injected volume	Description
24 May	75 L	Hydraulic fracturing
25 May – p1	77 L	Flow through fracture
25 May – p2	121 L	Flow through fracture

Table S1: Hydraulic stimulation protocol under study, stimulation carried out at the notch at 50-meter depth on the injection well E1-I.

Manuscript under review